JACS
JOURNAL OF THE AMERICAN CHEMICAL SOCIETY
pubs.acs.org/JACS

Article

Photoinduced Electron−Nuclear Dynamics of Fullerene and Its Monolayer Networks in Solvated Environments

Qiang Xu,* Daniel Weinberg, Mahmut Sait Okyay, Min Choi, Mauro Del Ben, and Bryan M. Wong*

Cite This: J. Am. Chem. Soc. 2024, 146, 35313−35320

Read Online

ACCESS | Metrics & More | Article Recommendations

ABSTRACT: The recently synthesized monolayer fullerene network in a quasi-hexagonal phase (qHP-C_{60}) exhibits superior electron mobility and optoelectronic properties compared to molecular fullerene (C_{60}), making it highly promising for a variety of applications. However, the microscopic carrier dynamics of qHP-C_{60} remain unclear, particularly in realistic environments, which are of significant importance for applications in optoelectronic devices. Unfortunately, traditional *ab initio* methods are prohibitive for capturing the real-time carrier dynamics of such large systems due to their high computational cost. In this work, we present the first real-time electron−nuclear dynamics study of qHP-C_{60} using velocity-gauge density functional tight binding, which enables us to perform several picoseconds of excited-state electron−nuclear dynamics simulations for nanoscale systems with periodic boundary conditions. When applied to C_{60}, qHP-C_{60}, and their solvated counterparts, we demonstrate that water/moisture significantly increases the electron−hole recombination time in C_{60} but has little impact on qHP-C_{60}. Our excited-state electron−nuclear dynamics calculations show that qHP-C_{60} is extremely unique and enable exploration of time-resolved dynamics for understanding excited-state processes of large systems in complex, solvated environments.

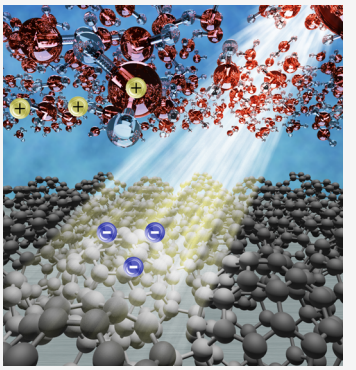

INTRODUCTION

The recently synthesized two-dimensional, monolayer fullerene network in a quasi-hexagonal phase (qHP-C_{60}) has attracted significant attention from the scientific community due to its favorable optical bandgap, superior electron mobility, and optoelectronic properties,[1] making it promising for broad applications in microelectronics, photovoltaics, and photocatalysis.[2−6] However, the performance of qHP-C_{60} in realistic environments is still unknown, particularly in the presence of water/moisture, which is typically present during solar cell fabrication and operation. As a closely related example, recent studies on perovskites have shown impressive performance in photovoltaic applications; however, their efficiencies significantly decrease when exposed to humidity, which degrades the material and reduces the performance of the device.[7−9] Similarly, understanding the excited-state dynamics (i.e., photogenerated electrons and holes) of qHP-C_{60} under realistic solvated/moisture environments is essential for realizing its potential technological applications.

Time-resolved measurements can enable unique insights into the intrinsic quantum dynamics of these chemical/material systems due to their ability to probe phenomena at the femtosecond[10] and attosecond[11] time scales. In particular, attosecond-resolution experiments, which recently garnered a 2023 Nobel prize,[11] have opened the door to exploring ultrafast excited-state electron(-nuclear) dynamics with exquisite precision.[12−15] These advanced experimental techniques have enabled the investigation of rich electron−nuclear dynamical effects, such as photoinduced phase transitions,[16,17] laser-induced hot-carrier transport dynamics,[18,19] and water-enhanced time scales in electron−hole recombination processes.[20,21] These findings provide insight into the underlying dynamic properties of charge carriers in these materials to guide the design of functional nanodevices.[18,22,23] However, experimental studies can only characterize a small portion of the photoinduced processes, and a deeper understanding of the carrier dynamics and the mechanisms behind these phenomena requires theoretical guidance and verification.[24]

In this work, we present a new Ehrenfest dynamics method, based on our recently developed velocity-gauge real-time time-dependent density functional tight-binding (VG-rtTDDFTB) approach,[25] for simulating excited-state electron−nuclear dynamics in large, complex, periodic condensed matter systems. In addition, we propose and implement an excited-state diagnostic for extracting real-time electron−hole pair distributions during the ensuing electron−nuclear dynamics. Our new approach provides a real-time and direct approach to observing electron−hole generation, transfer, and recombination. Using

Received: September 17, 2024
Revised: November 11, 2024
Accepted: November 25, 2024
Published: December 9, 2024

https://doi.org/10.1021/jacs.4c12952
J. Am. Chem. Soc. 2024, 146, 35313−35320

our new implementation, we perform extremely long, picosecond electron−nuclear dynamics simulations for molecular fullerene (C_{60}), qHP-C_{60},[1] and their solvated counterparts. These simulations are well beyond the capabilities and scope of traditional adiabatic Born−Oppenheimer molecular dynamics (BOMD) simulations or conventional time-dependent density functional theory (TDDFT), especially for large periodic nanoscale systems and long picosecond time scales. These massive simulations provide essential insight into solvent-mediated electron−nuclear dynamics and give a wholistic approach for exploring excited-state processes, such as hot carrier transport in nanomaterials,[21−23] in realistic environments.

THEORETICAL FORMALISM

To derive the coupled equations of motion for both the electrons and nuclei, we first construct the Lagrangian within the VG-rtTDDFTB formalism (setting $\hbar = e = m_e = 1$):

$$\mathcal{L} = \sum_I \frac{1}{2} M_I \dot{\mathbf{R}}_I^2 + \frac{1}{c} \sum_I Z_I \dot{\mathbf{R}}_I \cdot \mathbf{A} + \sum_{n\mathbf{k}}^{\text{Occ.}} \langle \psi_{n\mathbf{k}} | i \frac{\partial}{\partial t} - \hat{H}[\rho_0] - \hat{H}_{\text{ext}} | \psi_{n\mathbf{k}} \rangle - E_2[\Delta\mathbf{q}] - E_{\text{rep}}(\mathbf{R}) \tag{1}$$

where M_I, $\dot{\mathbf{R}}_I$, and Z_I are the mass, velocity, and charge of the Ith atomic nucleus, respectively. $\mathbf{A}(t) = -c\int_0^t \mathbf{E}(\tau)\mathrm{d}\tau$ is the real-time external vector potential, where c and $\mathbf{E}$ are the speed of light in vacuum and the external electric field, respectively. $\hat{H}[\rho_0]$ is the zeroth-order Hamiltonian that depends on the superposition of atomic densities, ρ_0; $E_2[\Delta\mathbf{q}] = \frac{1}{2}\sum_{IJ}\gamma_{IJ}\Delta q_I \Delta q_J$ and $E_{\text{rep}}(\mathbf{R})$ are the second-order correction energy and repulsive energy, respectively, where γ_{IJ} is the interaction coefficient that depends on the distance between the Ith and Jth atoms. The $\Delta\mathbf{q} = \{\Delta q_I\}$ and $\mathbf{R} = \{\mathbf{R}_I\}$ terms denote the sets of atomic Mulliken charges and positions, respectively.[25−28] In the long-wavelength approximation,[29−31] the external-field Hamiltonian, $\hat{H}_{\text{ext}}$, in the velocity gauge is given by[25]

$$\hat{H}_{\text{ext}}(t) = \frac{1}{c}\mathbf{A}(t)\cdot\hat{\mathbf{p}} + \frac{1}{2c^2}|\mathbf{A}(t)|^2 \tag{2}$$

where $\hat{\mathbf{p}}$ denotes the momentum operator. In the density functional tight-binding (DFTB)[26,27] formalism, a nonorthogonal pseudoatomic basis set, $\{|\phi_\mu^\zeta\rangle\}$, is used to discretize eq 1. The collective index, μ, represents (I, l, m) such that $|\phi_\mu^\zeta\rangle$ denotes the orbital centered on the Ith atom of the ζth periodic cell image in real space with (l, m) angular momentum quantum numbers, where $\phi_\mu(\mathbf{r} - \mathbf{R}_I - \mathbf{L}_\zeta) = \langle \mathbf{r}|\phi_\mu^\zeta\rangle$; $\mathbf{R}_I$ and $\mathbf{L}_\zeta$ are the positions of the Ith atom and ζth periodic image, respectively.[25] Using this atomic basis set, the Bloch state $|\psi_{n\mathbf{k}}\rangle$ in eq 1 can be rewritten as

$$|\psi_{n\mathbf{k}}\rangle = \frac{1}{\sqrt{N_\mathbf{k}}}\sum_\zeta \sum_{\mu=1}^{N_b} C_{n\mathbf{k}}^\mu e^{i\mathbf{k}\cdot\mathbf{L}_\zeta}|\phi_\mu^\zeta\rangle \tag{3}$$

where N_b is the number of atomic basis functions in the unit cell. Combining eqs 1 and 3, one can derive the dynamical equations for the electrons and nuclei via the Euler−Lagrange equations[32,33]:

$$\dot{\mathbf{C}}_{n\mathbf{k}} = -i\mathbf{S}_\mathbf{k}^{-1}(\mathbf{H}_\mathbf{k} - i\boldsymbol{\Gamma}_\mathbf{k})\mathbf{C}_{n\mathbf{k}} \tag{4}$$

$$\begin{aligned} M_I\ddot{\mathbf{R}}_I = & -\sum_\mathbf{k}\left[\mathrm{Tr}\left(\mathbf{D}_\mathbf{k}\nabla_I\mathbf{H}_\mathbf{k}^0 + \nabla_I\mathbf{S}_\mathbf{k}\sum_J\gamma_{IJ}\Delta q_J\right)\right. \\ & \left. + \mathrm{Tr}(\mathbf{D}_\mathbf{k}\nabla_I\mathbf{S}_\mathbf{k}\mathbf{S}_\mathbf{k}^{-1}\mathbf{H}_\mathbf{k}^{\text{ext}} + \text{h. c.})\right] \\ & -\frac{1}{c}Z_I\dot{\mathbf{A}} - \Delta q_I\sum_J\nabla_I\gamma_{IJ}\Delta q_J - \nabla_I E_{\text{rep}}(\mathbf{R}) \\ & -\sum_k \mathrm{Tr}(\mathbf{D}_\mathbf{k}\nabla_I\mathbf{S}_\mathbf{k}\mathbf{S}_\mathbf{k}^{-1}\mathbf{H}_\mathbf{k} + \text{h. c.}) \\ & -i\sum_\mathbf{k}[\mathrm{Tr}(\mathbf{D}_\mathbf{k}\nabla_I\mathbf{S}_\mathbf{k}\mathbf{S}_\mathbf{k}^{-1}\boldsymbol{\Gamma}_\mathbf{k} + \text{h. c.}) \\ & -\mathrm{Tr}(\mathbf{D}_\mathbf{k}\boldsymbol{\Theta}_{I,\mathbf{k}} + \text{h. c.})] \end{aligned} \tag{5}$$

where $\mathbf{C}_{n\mathbf{k}} = [C_{n\mathbf{k}}^1, C_{n\mathbf{k}}^2, \cdots]^T$ in eq 4 is the coefficient vector of the $n\mathbf{k}$th state; $\mathbf{D}_\mathbf{k} = \frac{1}{N_\mathbf{k}}\sum_n^{\text{occ.}}\mathbf{C}_{n\mathbf{k}}\mathbf{C}_{n\mathbf{k}}^\dagger$, $\mathbf{S}_\mathbf{k}$, $\mathbf{H}_\mathbf{k}^0$, $\mathbf{H}_\mathbf{k}^{\text{ext}}$, and $\mathbf{H}_\mathbf{k}$ denote the $\mathbf{k}$-dependent density, overlap, zero-order Hamiltonian, external Hamiltonian, and total Hamiltonian matrices, respectively.[25] The "h.c." abbreviation denotes the Hermitian conjugate of the terms in the parentheses. $\boldsymbol{\Gamma}_\mathbf{k}$ and $\boldsymbol{\Theta}_{I,\mathbf{k}}$ are the nonadiabatic coupling matrices, whose elements are given by

$$\Gamma_\mathbf{k}^{\mu\nu} = \sum_\zeta e^{-i\mathbf{k}\cdot\mathbf{L}_\zeta}\langle\phi_\mu^\zeta|\dot{\phi}_\nu^0\rangle \equiv \sum_\zeta e^{-i\mathbf{k}\cdot\mathbf{L}_\zeta}\overline{\Gamma}^{\mu\nu}(\mathbf{L}_\zeta) \tag{6}$$

$$\Theta_{I,\mathbf{k}}^{\mu\nu} = \sum_\zeta e^{-i\mathbf{k}\cdot\mathbf{L}_\zeta}\langle\nabla_I\phi_\mu^\zeta|\dot{\phi}_\nu^0\rangle \equiv \sum_\zeta e^{-i\mathbf{k}\cdot\mathbf{L}_\zeta}\overline{\Theta}_I^{\mu\nu}(\mathbf{L}_\zeta) \tag{7}$$

Note that the last line in eq 5 depends on the velocity of the nuclei, $|\dot{\phi}_\nu^0\rangle = |\nabla_J\phi_\nu^0\rangle\cdot\dot{\mathbf{R}}_J$, and contributes to the nonadiabatic coupling forces. The velocity-dependent forces are ignored in our implementation for the small nuclear velocities in the systems explored in our work.[28] Alternatively, the equation of motion in eq 4 can also be rewritten using the density matrix:

$$\dot{\mathbf{D}}_\mathbf{k} = -i\mathbf{S}_\mathbf{k}^{-1}(\mathbf{H}_\mathbf{k} - i\boldsymbol{\Gamma}_\mathbf{k})\mathbf{D}_\mathbf{k} + \text{h. c.} \tag{8}$$

Given initial conditions $\mathbf{D}_\mathbf{k}(0)$, $\mathbf{R}(0)$, and $\dot{\mathbf{R}}(0)$, one can simulate the real-time motion of both nuclei and electrons via eqs 5 and 8, respectively, where the time-dependent density matrix and nuclear coordinates are updated by the leapfrog[25] and Verlet[34] integral algorithms, respectively. The leapfrog method for propagating the electronic density matrix is computationally efficient for large matrices due to its fewer matrix multiplications, whereas the Verlet method is commonly applied to nuclear dynamics to ensure numerical stability and time-reversibility.

RESULTS AND DISCUSSION

Computational Details. We used fixed cell dimensions of 17.0 Å × 17.0 Å × 17.0 Å for both the isolated C_{60} and water-solvated fullerene (C_{60}-H_2O) systems. To capture a realistic solvated environment, we used a 1 g/cm^3 water-molecular density for the C_{60}-H_2O system, which resulted in a large system size of 450 atoms. We used an 18.4 Å × 15.9 Å × 17.0 Å box for the 2 × 1 × 1 supercell of qHP-C_{60},[1,35] as well as its solvated form (qHP-C_{60}-H_2O), which contains 426 atoms. All DFTB-based calculations, including ground-state calculations, geometry optimizations, BOMD simulations, electron dynamics, and Ehrenfest dynamics, used the *mio*-1−1 Slater-Koster parameter

https://doi.org/10.1021/jacs.4c12952
J. Am. Chem. Soc. 2024, 146, 35313−35320

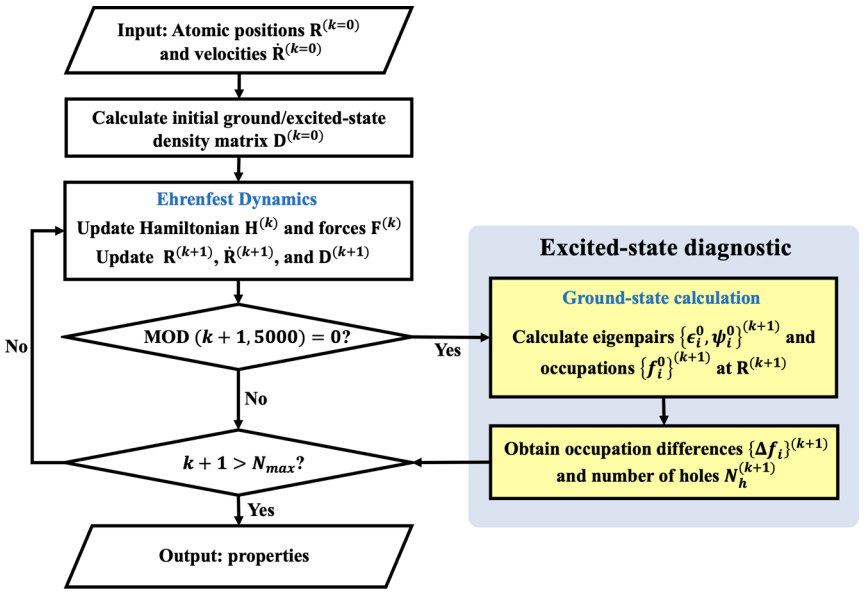

Figure 1. Flowchart of real-time Ehrenfest VG-rtTDDFTB with an excited-state diagnostic algorithm for extracting real-time electron−hole pair distributions.

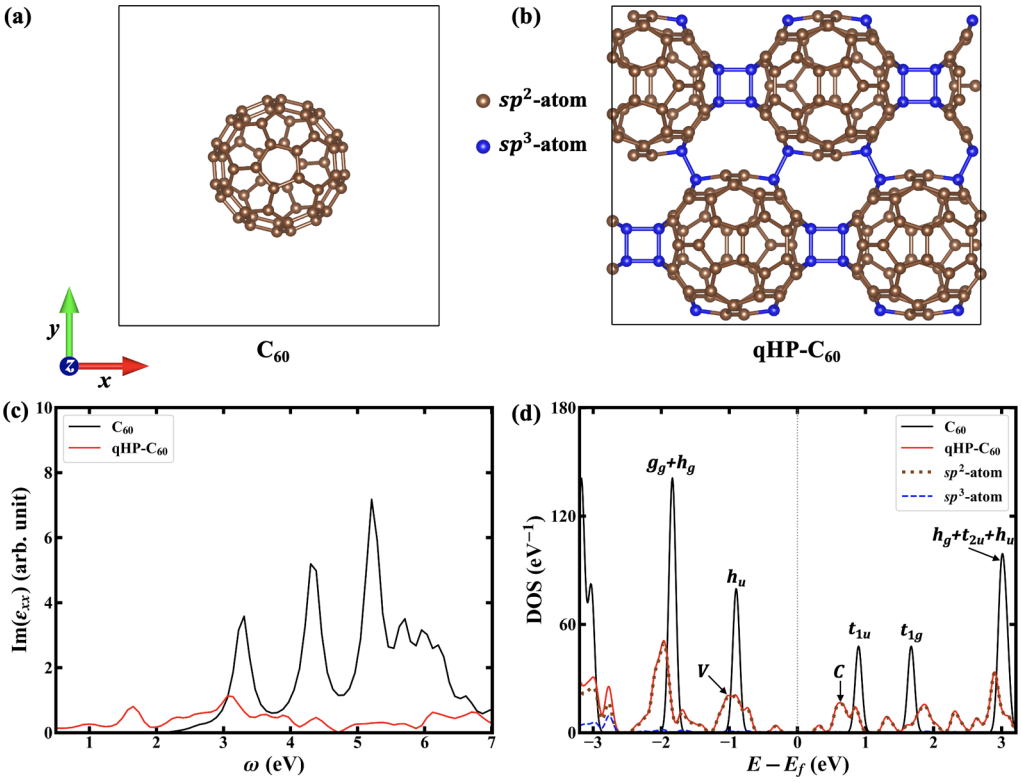

Figure 2. Geometries of (a) fullerene (C_{60}) and (b) quasi-hexagonal phase monolayer polymeric fullerene (qHP-C_{60}); the brown and blue spheres represent sp^2 and sp^3-hybridized carbon atoms, respectively. (c) Imaginary part of the dielectric function, ϵ_{xx}, and (d) DOS calculated with DFTB. The *g* and *u* subscripts in the DOS plot for C_{60} denote orbitals with gerade and ungerade symmetry, respectively. The *V* and *C* labels in the DOS plot for qHP-C_{60} denote valence- and conduction-band states at −1.0 and 0.7 eV, respectively.

set[26] with a single Γ point. A 0.5 and a 0.001 fs time step was used for our BOMD and electron/Ehrenfest dynamics, respectively. To obtain the time-dependent currents and absorption spectra,[25] we applied a δ-function electric field kick along the *x*-axis ($E_x(t) = E_0\delta(t)$ and E_0 = 0.005 eV/Å) for 50 fs (50,000 steps) on the optimized structures. Before starting the excited-state Ehrenfest dynamics simulations, we conducted an initial 10 ps (20,000 steps) of NVT-ensemble BOMD simulations, controlled by a Nosé-Hoover thermostat[36,37] at 300 K, to equilibrate all of the systems. We then performed excited-state Ehrenfest dynamics simulations, as shown in Figure 1. The initial conditions, $\mathbf{R}(0)$ and $\dot{\mathbf{R}}(0)$, for the Ehrenfest dynamics were obtained from the atomic positions and velocities of the last BOMD step, respectively. For the

https://doi.org/10.1021/jacs.4c12952
J. Am. Chem. Soc. 2024, 146, 35313−35320

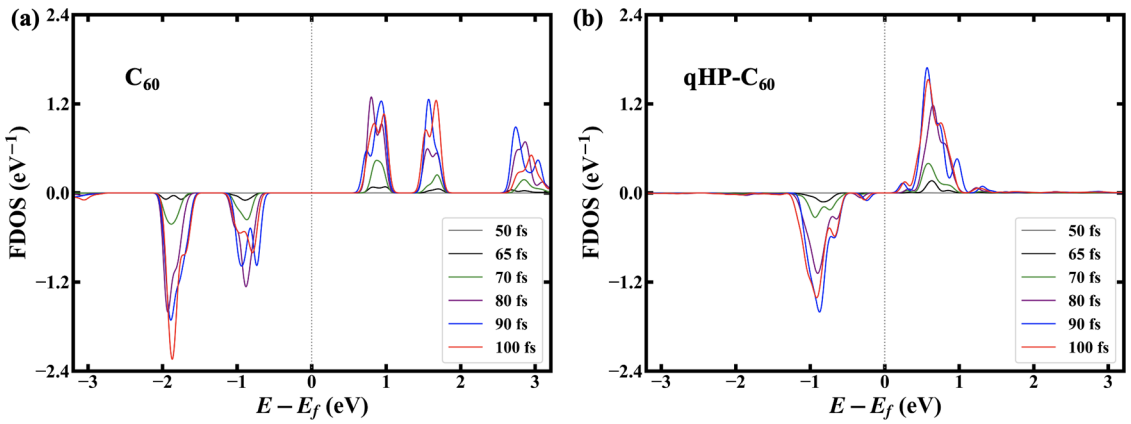

Figure 3. Time-resolved FDOS of (a) C_{60} and (b) qHP-C_{60} calculated by excited-state Ehrenfest dynamics at 300 K from 50 to 100 fs.

excited-state Ehrenfest dynamics, we applied a $\sin^2$-envelope laser pulse (centered at 75 fs) from 50 to 100 fs with an intensity of 10^{11} W/cm^2 ($E_0 \approx 0.0868$ eV/Å) along the x-axis for all systems. It is worth mentioning that our approach can also be initiated in an excited state rather than using an applied electric field, as indicated in the second box on the left side of our flowchart in Figure 1. Over 5 ps (>5,000,000 steps) of Ehrenfest dynamics were performed to capture the long-timescale excited electron−hole generation, transfer, and recombination processes.

In the remainder of this work, we simplify our notation for the index of states ($n\mathbf{k} \rightarrow i$) and omit the $\mathbf{k}$ index in the Hamiltonian and density matrices in Figure 1. To obtain dynamical information on the electronic-excited states, we also carried out a ground-state calculation at every 5,000 steps of the Ehrenfest dynamics trajectory with an external excited-state diagnostic code, as shown in the blue box of Figure 1, where $\epsilon_i^0(t)$, $\psi_i^0(t)$, and $f_i^0(t)$ are the ith eigenvalue, eigenstate, and occupation number for the ground-state Hamiltonian at time t, respectively. The electronic populations with respect to the ground-state occupations were calculated with the expression:

$$\Delta f_i(t) \equiv \langle \psi_i^0(t) | \hat{\mathbf{D}}(t) | \psi_i^0(t) \rangle - f_i^0(t) \tag{9}$$

where $\hat{\mathbf{D}}(t)$ is the real-time density matrix operator. Using $\{\Delta f_i(t)\}$, we can monitor the number of excited electrons (N_e) and holes (N_h) in real time with the expression $N_h(t) = N_e(t) = \frac{1}{2}\sum_{i=1}^{N_b} |\Delta f_i(t)|$. It is worth noting that this definition of N_h (or N_e) includes the contribution of intermediate states during the electron−hole generation/recombination process, which goes beyond traditional single-particle-state population analyses[38−41] and theoretical models.[42−46] To analyze the distribution of excited electrons and holes as a function of energy and time, we define a *time-resolved* Δf-factored density of states (FDOS) given by

$$\mathrm{FDOS}(E;t) \equiv \sum_{i=1}^{N_b} \Delta f_i(t) \delta[E - \epsilon_i^0(t)] \tag{10}$$

The density of states (DOS) and FDOS in this work were calculated with a Gaussian function with a width of 0.05 eV, and the Fermi level (E_f) in the DOS/FDOS was shifted to a 0 eV reference energy. To allow a direct comparison with C_{60}, the DOS, FDOS, N_h, and net charge transfer (ΔQ) for qHP-C_{60} were averaged over each C_{60} unit. The charge density[25] in this work was defined as $\rho(\mathbf{r}, t) \equiv \sum_I \frac{Q_I(t)}{\sqrt{(2\pi)^3}\eta^3} e^{-(\mathbf{r}-\mathbf{R}_I)^2/2\eta^2}$, where $Q_I(t) = Z_I - q_I(t)$ denotes the net charge on the Ith atom, and η is set to 0.5 Å.

Results. Before performing excited-state Ehrenfest dynamics calculations, we first calculated the optical spectra of C_{60} (Figure 2a) and monolayer polymeric fullerene, qHP-C_{60} (Figure 2b). As shown in Figure 2c, the absorption peaks of C_{60} calculated by our VG-rtTDDFTB approach are close to those obtained via linear-response TDDFT.[47] In addition, the low-energy absorption peaks at 1.02 and 1.65 eV for qHP-C_{60} are close to those obtained with TDDFT with the HSE06 functional.[48] Interestingly, we observed that the spectral onset appears at significantly different energies for the first main peaks in qHP-C_{60} (1.65 eV) and C_{60} (3.30 eV). To explore the origin of this difference, Figure 2d plots the DOS of C_{60} and qHP-C_{60}. The electronic excitations of C_{60} with sp^2-hybridized atoms obey the selection rule of allowed transitions only between gerade and ungerade states. As such, the C_{60} absorption peak at 3.30 eV is due to $g_g + h_g \rightarrow t_{1u}$ and $h_u \rightarrow t_{1g}$ electronic transitions due to the comparable energy-level differences between the states. On the other hand, the structure and orbital symmetry of qHP-C_{60} are significantly altered by the formation of sp^3-hybridized atoms.[35] The $V \rightarrow C$ electronic excitation is likely allowed for qHP-C_{60}, resulting in the first main absorption peak at 1.65 eV.

To provide further insight into these results, Figure 3 plots the FDOS for both C_{60} and qHP-C_{60}, which we obtained from excited-state Ehrenfest dynamics calculations using $\sin^2$-envelope laser pulses with frequencies of 3.30 and 1.65 eV for C_{60} and qHP-C_{60}, respectively. In the FDOS plots, we observed two main peaks corresponding to holes at the $g_g + h_g$ and h_u states below the Fermi level, whereas excited electrons appear at t_{1u}, t_{1g}, and $h_g + t_{2u} + h_u$ states above the Fermi level. The excited electrons in the higher-energy states ($h_g + t_{2u} + h_u$) can be attributed to second-order electronic transitions among the t_{1u}, t_{1g}, and $h_g + t_{2u} + h_u$ states. The FDOS of qHP-C_{60} in Figure 3b clearly demonstrates the transfer of electrons from the V states to the C states, in which both of these states have orbital contributions due to sp^2-hybridized atoms, as shown in Figure 2d. Therefore, the absorption peak of qHP-C_{60} at 1.65 eV is mainly caused by local bonding distortions among sp^2-hybridized atoms rather than the formation of sp^3-hybridized atoms.

As discussed in the Introduction, water/moisture can have a dramatic effect on electron−nuclear dynamics in complex material systems and can significantly alter electron emission,[49] electron−hole recombination,[20,21,46] and charge transfer.[24,50] While experiments have shown that water significantly affects

https://doi.org/10.1021/jacs.4c12952
J. Am. Chem. Soc. 2024, 146, 35313−35320

electron−hole recombination processes, a systematic, time-resolved analysis of these dynamic processes is less common due to the complexity of the excited-state dynamics in these large, disordered systems. To shed mechanistic insight into these processes, we carried out BOMD simulations of C_{60}-H_2O and qHP-C_{60}-H_2O (Figure 4a,b) shows structures from the last step of these BOMD simulations) followed by over 5 ps of excited-state Ehrenfest dynamics to calculate electron−hole dynamics.

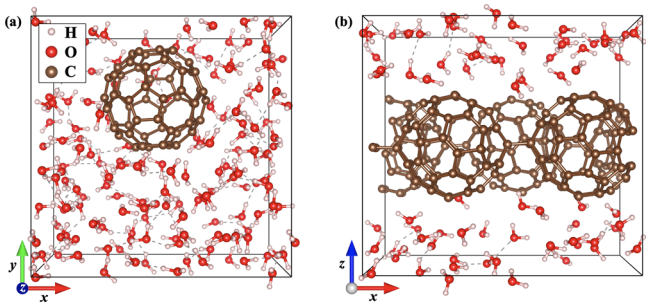

Figure 4. Structures of (a) C_{60}-H_2O and (b) qHP-C_{60}-H_2O obtained from the last step of 10 ps NVT molecular dynamics simulations.

To probe the underlying mechanisms of the exceptionally long time scales of excited electrons/holes in C_{60}-H_2O and qHP-C_{60}-H_2O, Figure 5 plots time-resolved charge density differences between the excited ($\rho(\mathbf{r}, t)$) and ground ($\rho_0(\mathbf{r}, t)$) states. During the interaction with the laser pulse between 50 and 100 fs, C_{60} generates a significant number of excited electron−hole pairs, coinciding with the transfer of a few holes to the adjacent water molecules. From 100 to 200 fs, the number of holes transferred to the nearby water molecules gradually increases. At 500 fs, the water molecules capture almost all of the holes in the system. Due to thermal fluctuations in the system, the holes diffuse to areas farther away from C_{60} after 500 fs. We observed similar hole-transfer and diffusion phenomena in qHP-C_{60}-H_2O, as shown in Figure 6. Furthermore, the excited electrons are concentrated on the surface of qHP-C_{60} after 1 ps, revealing more details of charge transfer at the water-matter interface.

To provide a more quantitative analysis of these charge-transfer dynamics, we used our new excited-state diagnostic algorithm to extract real-time electron−hole pair distributions from our Ehrenfest dynamics calculations. Figure 7a depicts the time-resolved number of holes (N_h) during this electron−hole combination process, which shows C_{60}-H_2O containing a large number of long-lived excited electrons and holes compared to C_{60}. In qHP-C_{60}-H_2O, as shown in Figure 7b, water also increases the electron−hole recombination lifetime, but the effect is small. The enhanced lifetimes of excited states are consistent with the charge dynamics in Figures 5 and 6 because the diffusion of water molecules with hole traps decreases the interaction between holes and electrons on C_{60}/qHP-C_{60}, which will increase the electron−hole recombination time scales. These findings also indicate that qHP-C_{60} is a promising functional material that can retain its intrinsic electronic properties (as opposed to perovskites, whose performance changes in the presence of moisture) even in complex environments present in realistic electronic devices. To further explore the differences between these two systems, Figure 7c,d plots the real-time charge-transfer dynamics of C_{60}-H_2O and qHP-C_{60}-H_2O, respectively. The results clearly show that the number of holes transferred to water by qHP-C_{60} (per C_{60} unit) is only 1/5 of that of C_{60}, which confirms that water has a minor impact on the charge-transfer dynamics of the qHP-C_{60} system. This effect is also due to the 2-dimensional thin film of qHP-C_{60} having a smaller specific surface area at the water-matter interface compared to the 0-dimensional C_{60}, which significantly reduces hole transfer and the formation of hole traps on the surrounding water molecules. As shown in Figure 6, only the outermost carbon atoms in the qHP-C_{60}-water interface can

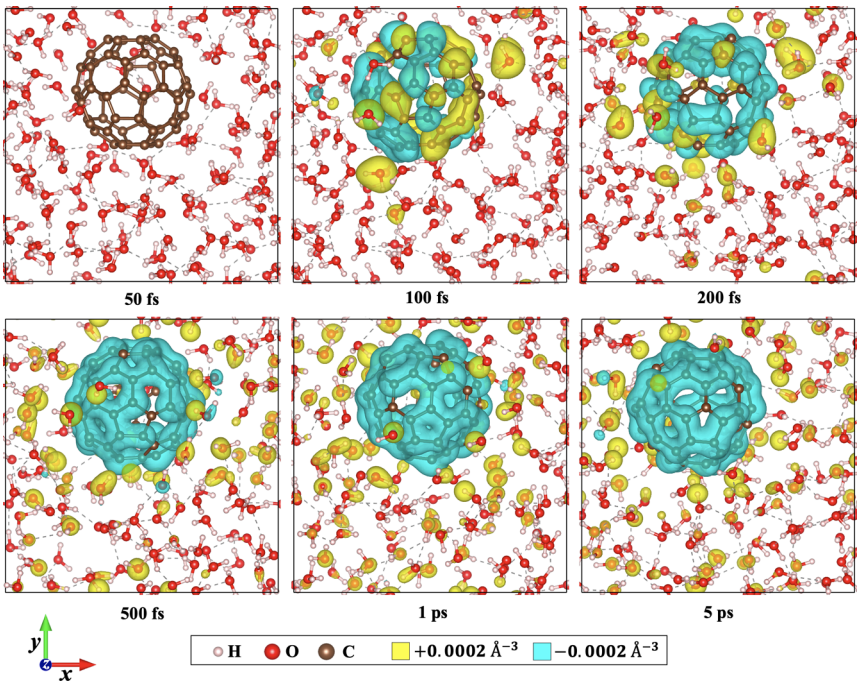

Figure 5. Snapshots of laser-induced charge density fluctuations $\Delta\rho(\mathbf{r}, t) \equiv \rho(\mathbf{r}, t) - \rho_0(\mathbf{r}, t)$, where $\rho_0(\mathbf{r}, t)$ is the ground-state charge density, for C_{60} in a periodic box of water calculated with VG-rtTDDFTB-based Ehrenfest dynamics. The simulations were carried out at 300 K for 5 ps.

https://doi.org/10.1021/jacs.4c12952
J. Am. Chem. Soc. 2024, 146, 35313−35320

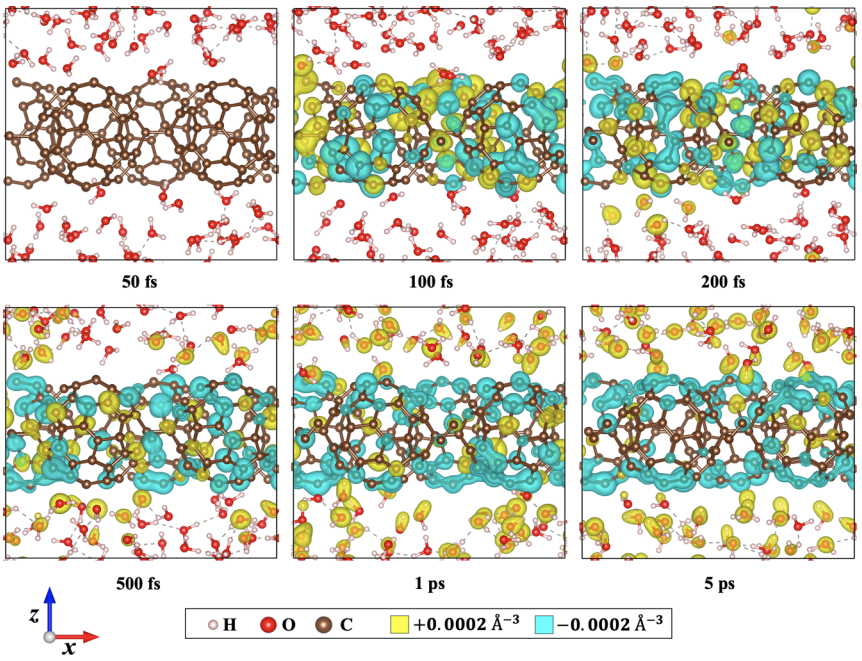

Figure 6. Snapshots of laser-induced charge density fluctuations $\Delta\rho(\mathbf{r}, t) \equiv \rho(\mathbf{r}, t) - \rho_0(\mathbf{r}, t)$, where $\rho_0(\mathbf{r}, t)$ is the ground-state charge density, for qHP-C_{60} in a periodic box of water calculated with VG-rtTDDFTB-based Ehrenfest dynamics. The simulations were carried out at 300 K for 5 ps.

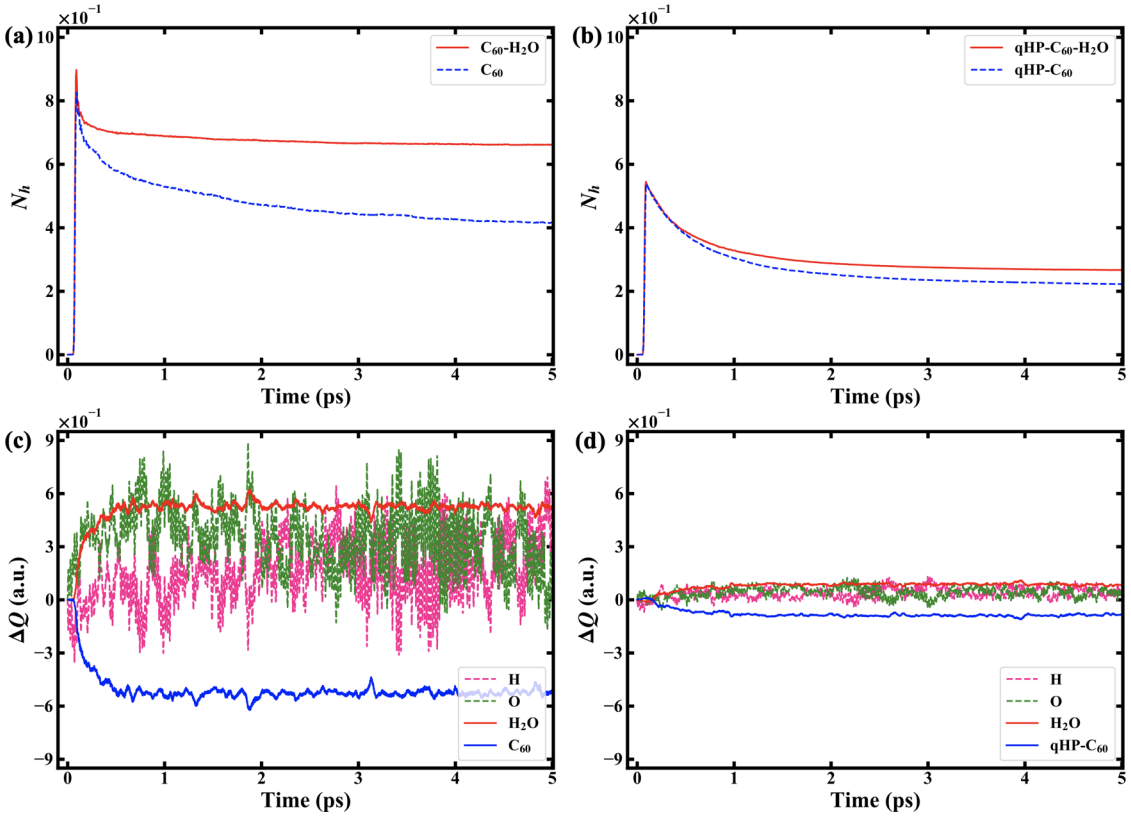

Figure 7. Time-resolved number of holes in (a) C_{60}, C_{60}-H_2O, and (b) qHP-C_{60}, qHP-C_{60}-H_2O. Real-time net charge transfer, $\Delta Q(t) = Q(t) - Q(0)$, in (c) C_{60}-H_2O and (d) qHP-C_{60}-H_2O calculated from Ehrenfest VG-rtTDDFTB dynamics.

interact with water molecules and accept electrons; however, the internal and sp^3-hybridized carbon atoms of qHP-C_{60} are inactive for hole transfer, as shown by the yellow-colored hole densities located inside qHP-C_{60} after 500 fs. In contrast, all of the carbon atoms in C_{60} interact with the surrounding water molecules (and their electrons) as shown in Figure 5 after 500 fs.

Overall, our excited-state electron−nuclear simulations provide mechanistic details of these hole-trap processes and an intuitive physical picture for understanding excited-state lifetimes and solvent-mediated electron−nuclear dynamics in large, complex systems.

https://doi.org/10.1021/jacs.4c12952
J. Am. Chem. Soc. 2024, 146, 35313−35320

CONCLUSIONS

In summary, we have developed and applied a new Ehrenfest VG-rtTDDFTB approach for probing laser-induced excited-state electron−nuclear dynamics of large systems with picosecond-long time scales. This new capability enables a holistic approach for capturing time-resolved, excited-state electron−nuclear dynamics, including excited electron−hole generation/transfer and nonradiative recombination processes in a variety of condensed phase systems. As representative examples of our approach, we calculated absorption spectra and time-resolved electron transitions for both C_{60} and qHP-C_{60}. We found that local bonding distortion plays a significant role in the different low-energy-excitation dynamics observed in C_{60} and qHP-C_{60}. Moreover, we carried out over 5 ps of electron−nuclear dynamics simulations (more than 5,000,000 steps) for solvated systems of C_{60} and qHP-C_{60}, containing 450 and 426 atoms, respectively. We observed that water significantly increases the electron−hole recombination time scales in C_{60} but has little impact on qHP-C_{60} due to the generation and diffusion of hole traps in the individual water molecules. These large-scale/long-time-scale simulations allow us to rationalize the absorption spectra and electron transitions in these systems to offer mechanistic insight into solvent-mediated electron−nuclear dynamics in condensed-phase systems. Finally, our approach provides a comprehensive paradigm for exploring time-resolved electron−nuclear dynamics to understand excited-state dynamics of large chemical/material systems in realistic environments.

AUTHOR INFORMATION

Corresponding Authors

Qiang Xu − *Department of Chemistry, Department of Physics and Astronomy, and Materials Science and Engineering Program, University of California-Riverside, Riverside, California 92521, United States;* orcid.org/0000-0003-3747-4325; Email: qiangx@ucr.edu

Bryan M. Wong − *Department of Chemistry, Department of Physics and Astronomy, and Materials Science and Engineering Program, University of California-Riverside, Riverside, California 92521, United States;* orcid.org/0000-0002-3477-8043; Email: bryan.wong@ucr.edu

Authors

Daniel Weinberg − *Applied Mathematics and Computational Research Division, Lawrence Berkeley National Laboratory, Berkeley, California 94720, United States;* orcid.org/0000-0001-7552-4712

Mahmut Sait Okyay − *Department of Chemistry, Department of Physics and Astronomy, and Materials Science and Engineering Program, University of California-Riverside, Riverside, California 92521, United States*

Min Choi − *Department of Chemistry, Department of Physics and Astronomy, and Materials Science and Engineering Program, University of California-Riverside, Riverside, California 92521, United States*

Mauro Del Ben − *Applied Mathematics and Computational Research Division, Lawrence Berkeley National Laboratory, Berkeley, California 94720, United States*

Complete contact information is available at: https://pubs.acs.org/10.1021/jacs.4c12952

Notes

The authors declare no competing financial interest.

ACKNOWLEDGMENTS

This work was supported by the U.S. Department of Energy, Office of Science, Office of Advanced Scientific Computing Research, Scientific Discovery through the Advanced Computing (SciDAC) program under Award Number DE-SC0022209. This research used resources of the National Energy Research Scientific Computing Center (NERSC), a U.S. Department of Energy Office of Science User Facility located at Lawrence Berkeley National Laboratory, operated under Contract No. DE-AC02-05CH11231 using NERSC award BES-ERCAP0023692.

REFERENCES

(1) Hou, L.; Cui, X.; Guan, B.; Wang, S.; Li, R.; Liu, Y.; Zhu, D.; Zheng, J. Synthesis of a Monolayer Fullerene Network. *Nature* **2022**, *606*, 507−510.

(2) Avouris, P.; Chen, Z.; Perebeinos, V. Carbon-Based Electronics. *Nature Nanotechnol.* **2007**, *2*, 605−615.

(3) Zhu, H.; Wei, J.; Wang, K.; Wu, D. Applications of Carbon Materials in Photovoltaic Solar Cells. *Sol. Energy Mater. Sol. Cells* **2009**, *93*, 1461−1470.

(4) Sahani, S.; Tripathi, K. M.; Lee, T. I.; Dubal, D. P.; Wong, C.-P.; Sharma, Y. C.; Kim, T. Y. Recent Advances in Photocatalytic Carbon-Based Materials for Enhanced Water Splitting under Visible-Light Irradiation. *Energy Convers. Manag.* **2022**, *252*, No. 115133.

(5) Bramhaiah, K.; Bhattacharyya, S. Challenges and Future Prospects of Graphene-Based Hybrids for Solar Fuel Generation: Moving Towards Next Generation Photocatalysts. *Mater. Adv.* **2022**, *3*, 142−172.

(6) Capobianco, A.; Wiktor, J.; Landi, A.; Ambrosio, F.; Peluso, A. Electron Localization and Mobility in Monolayer Fullerene Networks. *Nano Lett.* **2024**, *24*, 8335−8342.

(7) Hidalgo, J.; Kaiser, W.; An, Y.; Li, R.; Oh, Z.; Castro-Méndez, A.-F.; LaFollette, D. K.; Kim, S.; Lai, B.; Breternitz, J.; Schorr, S.; Perini, C. A. R.; Mosconi, E.; De Angelis, F.; Correa-Baena, J.-P. Synergistic Role of Water and Oxygen Leads to Degradation in Formamidinium-Based Halide Perovskites. *J. Am. Chem. Soc.* **2023**, *145*, 24549−24557.

(8) Ho, K.; Wei, M.; Sargent, E. H.; Walker, G. C. Grain Transformation and Degradation Mechanism of Formamidinium and Cesium Lead Iodide Perovskite under Humidity and Light. *ACS Energy Lett.* **2021**, *6*, 934−940.

(9) Kaiser, W.; Ricciarelli, D.; Mosconi, E.; Alothman, A. A.; Ambrosio, F.; De Angelis, F. Stability of Tin- versus Lead-Halide Perovskites: Ab Initio Molecular Dynamics Simulations of Perovskite/Water Interfaces. *J. Phys. Chem. Lett.* **2022**, *13*, 2321−2329.

(10) Zewail, A. H. Femtochemistry: Atomic-Scale Dynamics of the Chemical Bond Using Ultrafast Lasers (Nobel Lecture). *Angew. Chem., Int. Ed.* **2000**, *39*, 2586−2631.

(11) Leone, S. R. Profile of Pierre Agostini, Anne L'Huillier, and Ferenc Krausz: 2023 Nobel Laureates in Physics. *Proc. Natl. Acad. Sci. U. S. A.* **2024**, *121*, No. e2321587121.

(12) Leone, S. R.; McCurdy, C. W.; Burgdörfer, J.; Cederbaum, L. S.; Chang, Z.; Dudovich, N.; Feist, J.; Greene, C. H.; Ivanov, M.; Kienberger, R.; et al. What Will It Take to Observe Processes in 'real time'? *Nat. Photon.* **2014**, *8*, 162−166.

(13) Cavalieri, A. L.; Müller, N.; Uphues, T.; Yakovlev, V. S.; Baltuška, A.; Horvath, B.; Schmidt, B.; Blümel, L.; Holzwarth, R.; Hendel, S.; et al. Attosecond Spectroscopy in Condensed Matter. *Nature* **2007**, *449*, 1029−1032.

(14) Goulielmakis, E.; Loh, Z.-H.; Wirth, A.; Santra, R.; Rohringer, N.; Yakovlev, V. S.; Zherebtsov, S.; Pfeifer, T.; Azzeer, A. M.; Kling, M. F.; et al. Real-Time Observation of Valence Electron Motion. *Nature* **2010**, *466*, 739−743.

(15) Kraus, P. M.; Zürch, M.; Cushing, S. K.; Neumark, D. M.; Leone, S. R. The Ultrafast X-Ray Spectroscopic Revolution in Chemical Dynamics. *Nat. Rev. Chem.* **2018**, *2*, 82−94.

(16) Yen, R.; Liu, J.; Kurz, H.; Bloembergen, N. Space-Time Resolved Reflectivity Measurements of Picosecond Laser-Pulse Induced Phase Transitions in (111) Silicon Surface Layers. *Appl. Phys. A: Mater. Sci. Process.* **1982**, *27*, 153−160.
(17) Hervé, M.; Privault, G.; Trzop, E.; Akagi, S.; Watier, Y.; Zerdane, S.; Chaban, I.; Torres Ramírez, R. G.; Mariette, C.; Volte, A.; et al. Ultrafast and Persistent Photoinduced Phase Transition at Room Temperature Monitored by Streaming Powder Diffraction. *Nat. Commun.* **2024**, *15*, 267.
(18) Tagliabue, G.; DuChene, J. S.; Abdellah, M.; Habib, A.; Gosztola, D. J.; Hattori, Y.; Cheng, W.-H.; Zheng, K.; Canton, S. E.; Sundararaman, R.; et al. Ultrafast Hot-Hole Injection Modifies Hot-Electron Dynamics in Au/p-GaN Heterostructures. *Nat. Mater.* **2020**, *19*, 1312−1318.
(19) Taghinejad, M.; Xia, C.; Hrton, M.; Lee, K.-T.; Kim, A. S.; Li, Q.; Guzelturk, B.; Kalousek, R.; Xu, F.; Cai, W.; et al. Determining Hot-Carrier Transport Dynamics from Terahertz Emission. *Science* **2023**, *382*, 299−305.
(20) Schneider, J.; Matsuoka, M.; Takeuchi, M.; Zhang, J.; Horiuchi, Y.; Anpo, M.; Bahnemann, D. W. Understanding TiO_2 Photocatalysis: Mechanisms and Materials. *Chem. Rev.* **2014**, *114*, 9919−9986.
(21) Neelakanni Mudiyanselage, S.; Donnellan, Z.; Hoffmann, L.; Ghosh, S.; Qian, J.; Jamnuch, S.; Pascal, T.; Roth, F.; Eberhardt, W.; Gessner, O. Photo-Induced Plasmonic Light Harvesting Dynamics and Chemical Transformations Monitored Via Picosecond Time-Resolved Ambient-Pressure X-ray Photoelectron Spectroscopy (TRAPXPS). In *APS Division of Atomic, Molecular and Optical Physics Meeting Abstracts*, 2023; pp. M06-007.
(22) Dhama, R.; Habib, M.; Rashed, A. R.; Caglayan, H. Unveiling Long-Lived Hot-Electron Dynamics via Hyperbolic Meta-Antennas. *Nano Lett.* **2023**, *23*, 3122−3127.
(23) Yannai, M.; Dahan, R.; Gorlach, A.; Adiv, Y.; Wang, K.; Madan, I.; Gargiulo, S.; Barantani, F.; Dias, E. J.; Vanacore, G. M.; et al. Ultrafast Electron Microscopy of Nanoscale Charge Dynamics in Semiconductors. *ACS Nano* **2023**, *17*, 3645−3656.
(24) You, P.; Chen, D.; Liu, X.; Zhang, C.; Selloni, A.; Meng, S. Correlated Electron−Nuclear Dynamics of Photoinduced Water Dissociation on Rutile TiO_2. *Nat. Mater.* **2024**, *23*, 1100−1106.
(25) Xu, Q.; Del Ben, M.; Sait Okyay, M.; Choi, M.; Ibrahim, K. Z.; Wong, B. M. Velocity-Gauge Real-Time Time-Dependent Density Functional Tight-Binding for Large-Scale Condensed Matter Systems. *J. Chem. Theory Comput.* **2023**, *19*, 7989−7997.
(26) Elstner, M.; Porezag, D.; Jungnickel, G.; Elsner, J.; Haugk, M.; Frauenheim, T.; Suhai, S.; Seifert, G. Self-Consistent-Charge Density-Functional Tight-Binding Method for Simulations of Complex Materials Properties. *Phys. Rev. B* **1998**, *58*, 7260.
(27) Hourahine, B.; Aradi, B.; Blum, V.; Bonafé, F.; Buccheri, A.; Camacho, C.; Cevallos, C.; Deshaye, M.; Dumitrică, T.; Dominguez, A.; et al. DFTB+, a Software Package for Efficient Approximate Density Functional Theory Based Atomistic Simulations. *J. Chem. Phys.* **2020**, *152*, 124101.
(28) Bonafé, F. P.; Aradi, B.; Hourahine, B.; Medrano, C. R.; Hernández, F. J.; Frauenheim, T.; Sánchez, C. G. A Real-Time Time-Dependent Density Functional Tight-Binding Implementation for Semiclassical Excited State Electron−Nuclear Dynamics and Pump−Probe Spectroscopy Simulations. *J. Chem. Theory Comput.* **2020**, *16*, 4454−4469.
(29) Pemmaraju, C. D.; Vila, F. D.; Kas, J. J.; Sato, S. A.; Rehr, J. J.; Yabana, K.; Prendergast, D. Velocity-Gauge Real-Time TDDFT within a Numerical Atomic Orbital Basis Set. *Comput. Phys. Commun.* **2018**, *226*, 30−38.
(30) Mattiat, J.; Luber, S. Comparison of Length, Velocity, and Symmetric Gauges for the Calculation of Absorption and Electric Circular Dichroism Spectra with Real-Time Time-Dependent Density Functional Theory. *J. Chem. Theory Comput.* **2022**, *18*, 5513−5526.
(31) Ding, F.; Liang, W.; Chapman, C. T.; Isborn, C. M.; Li, X. On the Gauge Invariance of Nonperturbative Electronic Dynamics Using the Time-Dependent Hartree-Fock and Time-Dependent Kohn-Sham. *J. Chem. Phys.* **2011**, *135*, 164101.
(32) Todorov, T. Time-Dependent Tight Binding. *J. Phys.: Condens. Matter* **2001**, *13*, 10125.
(33) Niehaus, T. A.; Heringer, D.; Torralva, B.; Frauenheim, T. Importance of Electronic Self-Consistency in the TDDFT Based Treatment of Nonadiabatic Molecular Dynamics. *Eur. Phys. J. D.* **2005**, *35*, 467−477.
(34) Swope, W. C.; Andersen, H. C.; Berens, P. H.; Wilson, K. R. A Computer Simulation Method for the Calculation of Equilibrium Constants for the Formation of Physical Clusters of Molecules: Application to Small Water Clusters. *J. Chem. Phys.* **1982**, *76*, 637−649.
(35) Tromer, R. M.; Junior, L. A. R.; Galvão, D. S. A DFT Study of the Electronic, Optical, and Mechanical Properties of a Recently Synthesized Monolayer Fullerene Network. *Chem. Phys. Lett.* **2022**, *804*, No. 139925.
(36) Nosé, S. A Unified Formulation of the Constant Temperature Molecular Dynamics Methods. *J. Chem. Phys.* **1984**, *81*, 511−519.
(37) Hoover, W. G. Canonical dynamics: Equilibrium Phase-Space Distributions. *Phys. Rev. A* **1985**, *31*, 1695.
(38) Li, W.; Sun, Y.-Y.; Li, L.; Zhou, Z.; Tang, J.; Prezhdo, O. V. Control of Charge Recombination in Perovskites by Oxidation State of Halide Vacancy. *J. Am. Chem. Soc.* **2018**, *140*, 15753−15763.
(39) He, J.; Fang, W.-H.; Long, R. Unravelling the Effects of Oxidation State of Interstitial Iodine and Oxygen Passivation on Charge Trapping and Recombination in $CH_3NH_3PbI_3$ perovskite: a Time-Domain Ab Initio Study. *Chem. Sci.* **2019**, *10*, 10079−10088.
(40) Kim, T. W.; Jun, S.; Ha, Y.; Yadav, R. K.; Kumar, A.; Yoo, C.-Y.; Oh, I.; Lim, H.-K.; Shin, J. W.; Ryoo, R.; et al. Ultrafast Charge Transfer Coupled with Lattice Phonons in Two-Dimensional Covalent Organic Frameworks. *Nat. Commun.* **2019**, *10*, 1873.
(41) He, J.; Fang, W.-H.; Long, R.; Prezhdo, O. V. Why Oxygen Increases Carrier Lifetimes but Accelerates Degradation of $CH_3NH_3PbI_3$ under Light Irradiation: Time-Domain Ab Initio Analysis. *J. Am. Chem. Soc.* **2020**, *142*, 14664−14673.
(42) Shockley, W.; Read, W. T., Jr. Statistics of the Recombinations of Holes and Electrons. *Phys. Rev.* **1952**, *87*, 835.
(43) Zhang, J. Z. Ultrafast Studies of Electron Dynamics in Semiconductor and Metal Colloidal Nanoparticles: Effects of Size and Surface. *Acc. Chem. Res.* **1997**, *30*, 423−429.
(44) Grundmann, M. *Physics of Semiconductors*; Springer, 2010; Vol. *11*.
(45) Wei, H.; Luo, J.-W.; Li, S.-S.; Wang, L.-W. Revealing the Origin of Fast Electron Transfer in TiO_2-Based Dye-Sensitized Solar Cells. *J. Am. Chem. Soc.* **2016**, *138*, 8165−8174.
(46) Wang, S.; Huang, M.; Wu, Y.-N.; Chu, W.; Zhao, J.; Walsh, A.; Gong, X.-G.; Wei, S.-H.; Chen, S. Effective Lifetime of Non-Equilibrium Carriers in Semiconductors from Non-Adiabatic Molecular Dynamics Simulations. *Nat. Comput. Sci.* **2022**, *2*, 486−493.
(47) Niehaus, T. A.; Suhai, S.; Della Sala, F.; Lugli, P.; Elstner, M.; Seifert, G.; Frauenheim, T. Tight-Binding Approach to Time-Dependent Density-Functional Response Theory. *Phys. Rev. B* **2001**, *63*, No. 085108.
(48) Yuan, D.; Pi, H.; Jiang, Y.; Hu, Y.; Zhou, L.; Jia, Y.; Su, G.; Fang, Z.; Weng, H.; Ren, X.; et al. Highly In-Plane Anisotropic Optical Properties of Fullerene Monolayers. *Sci. China Phys. Mech. Astron.* **2023**, *66*, 247211.
(49) Devlin, S. W.; Jamnuch, S.; Xu, Q.; Chen, A. A.; Qian, J.; Pascal, T. A.; Saykally, R. J. Agglomeration Drives the Reversed Fractionation of Aqueous Carbonate and Bicarbonate at the Air−Water Interface. *J. Am. Chem. Soc.* **2023**, *145*, 22384−22393.
(50) Menzel, J. P.; Papadopoulos, A.; Belić, J.; de Groot, H. J.; Visscher, L.; Buda, F. Photoinduced Electron Injection in a Fully Solvated Dye-Sensitized Photoanode: A Dynamical Semiempirical Study. *J. Phys. Chem. C* **2020**, *124*, 27965−27976.

https://doi.org/10.1021/jacs.4c12952
J. Am. Chem. Soc. 2024, 146, 35313−35320